Hindawi
International Journal of Energy Research
Volume 2024, Article ID 4878549, 11 pages
https://doi.org/10.1155/2024/4878549

Research Article

Facile Synthesis of WS_2/WO_3 Materials in a Batch Reactor for the Hydrogen Evolution Reaction

Tuan Van Nguyen,[1] **Kim Anh Huynh**,[2] **Quyet Van Le**,[1] **Sang Hyun Ahn**,[3] **and Soo Young Kim**[1]

[1]*Department of Materials Science and Engineering, Institute of Green Manufacturing Technology, Korea University, 145 Anam-ro, Seongbuk-gu, Seoul 02841, Republic of Korea*
[2]*Department of Materials Science and Engineering, Gachon University, Seongnam, Gyeonggi-Do 13306, Republic of Korea*
[3]*School of Chemical Engineering and Materials Science, Chung-Ang University, 84 Heukseok-ro, Dongjak-gu, Seoul 06974, Republic of Korea*

Correspondence should be addressed to Sang Hyun Ahn; shahn@cau.ac.kr and Soo Young Kim; sooyoungkim@korea.ac.kr

Received 1 November 2023; Revised 18 December 2023; Accepted 29 April 2024; Published 16 May 2024

Academic Editor: Semen Klyamkin

In this study, a new and facile process was developed for the preparation of composite catalysts based on tungsten oxide (WO_3) by batch reactor routes. The structures, morphologies, compositions, and characteristics of synthesized materials were investigated and confirmed. Using batch reactor processes, WO_3 nanorods (WO_3 NR), heterostructures of WS_2/WO_3 nanobricks (WS_2/WO_3 NB), and WS_2/WO_3 nanorods (WS_2/WO_3 NR) were successfully prepared. The prepared materials were then employed for hydrogen evolution reaction (HER) to investigate their catalytic performance. The results indicated that the electrocatalytic activities of WS_2/WO_3 NR are significantly improved compared to those of WO_3 NR and WS_2/WO_3 NB. This improvement could be attributed to the formation of heterostructure between WS_2 and WO_3 elements in highly uniform materials, which could create the synergistic effect and further improve the catalytic activities of the catalyst. The data shows that the Tafel slope of WS_2/WO_3 NR (82.7 mV dec^{-1}) is significantly lower than that of WO_3 NR (112.5 mV dec^{-1}) and WS_2/WO_3 NB (195.5 mV dec^{-1}). Furthermore, the resistance of WS_2/WO_3 NR (397.7 Ω) is markedly decreased compared to those of WO_3 NR (1816 Ω) and WS_2/WO_3 NB (3597 Ω). The results indicate that WS_2/WO_3 NR could be a great catalyst for electrochemical applications.

1. Introduction

Over the last decades, the excessive use of fossil fuels has become a critical issue that must be addressed because of greenhouse gas emissions and global warming [1–5]. New materials and breakthrough technologies are increasingly necessary to conserve energy and develop environmentally friendly energy sources. Tremendous efforts have been made to overcome the emerging environmental problems [6–13]. With the advent of cutting-edge technologies, hydrogen is one of the most prominent candidates as an ecosystem-friendly and reusable energy source [14–21]. Different materials have been investigated to enhance reaction performance and produce hydrogen gas [22–28]. Thus far, noble metals such as Pt group metals have demonstrated higher active electrocatalyst performances for the hydrogen evolution reaction (HER) than other materials [29–32]. However, the scarcity and high cost of those catalysts are their major drawbacks. Therefore, the design of abundant, low-cost materials with excellent catalytic performance for HER applications remains a considerable challenge for researchers. Transition metals and their compounds are promising candidates for the preparation of excellent catalytic materials for the HER. Recently, transition metals and their compounds have been extensively investigated for HER performance because of their benefits for electrocatalyst materials [33–35]. Among many materials, the well-known transition metal W and its derivatives have distinctive electronic characteristics [36–38].

In particular, WO_3 has been extensively investigated for various applications such as electrochromic devices [39–41], sensors [42, 43], solar cells [44, 45], photocatalysts [46, 47], and HER applications [48–51].

Catalysts based on WO_3 exhibit poor catalytic properties because the adsorption energy of atomic hydrogen on WO_3 molecules is inadequate, resulting in the low activity of WO_3 for the HER in the electrolyte [52, 53]. This can be attributed to the low conductivity and intrinsic inactivity of WO_3. In recent decades, several approaches have been developed to improve the HER performance of WO_3, including metallic and non-metallic doping to form hybrid materials [54, 55]. Noble metal doping or hybrid materials may create synergistic effects between different elements that can tune the electronic structure, increase the number of catalytic active sites, and enhance the HER activity. However, noble metal doping has several limitations, including complicated processes and expensive materials [56, 57]. Therefore, numerous studies have been conducted to develop facile, scalable, and low-cost processes for the synthesis of heterostructure catalysts based on WO_3 materials [58–60]. In previous researches, the performance of different catalysts based on various structures of WO_3 and/or WS_2 is listed in Table S1.

Herein, a simple, low-cost, and scalable method is introduced to synthesize different structures of WO_3 and its derivatives using a batch reactor. Various measurements were conducted to confirm the formation and morphology of the synthesized materials. Different materials including WO_3 nanorods (WO_3 NR) and heterostructures of WS_2/WO_3 nanobricks (WS_2/WO_3 NB) and WS_2/WO_3 nanorods (WS_2/WO_3 NR) were prepared. Electrochemical studies demonstrated that the HER activity of WS_2/WO_3 NR was higher than those of WO_3 NR and WS_2/WO_3 NB. The highly uniform and synergistic effect of WS_2 and WO_3 elements in the synthesized WS_2/WO_3 NR could be responsible for its excellent HER performance. Based on the catalytic performance, the synthesized WS_2/WO_3 NR is a promising material for electrochemical applications.

2. Experimental Section

The experiments were conducted in a closed batch reactor. The different mechanisms of procedures are briefly illustrated in Section 2.6.

2.1. Materials. All materials were used as received, without further purification. Ammonium metatungstate hydrate ($(NH_4)_6H_2W_{12}O_{40}.xH_2O$) (AMT), thioacetamide (TAA) (C_2H_5NS, 99%), and hydrochloric acid (HCl, ACS reagent, 37%) were purchased from Sigma–Aldrich. Dimethylformamide (DMF) was supplied by Alfa Aesar. Deionized (DI) water (18.3 $M\Omega\,cm^{-1}$) was obtained from Millipore Milli-Q.

2.2. Synthesis of WO_3 NR. TAA (3.75 g) was dissolved and stirred for 30 min in DI water (25 mL) in a 100 mL Teflon beaker. Subsequently, AMT (4 g) was added to the prepared solution, followed by stirring continuously for 30 min. Then, the Teflon beaker was placed in a batch reactor system and heated at 180°C for 24 h. After cooling to room temperature, the precipitate was formed at the bottom of the Teflon beaker, and it was collected and centrifuged thrice with DI water. The obtained powder, WO_3 NR, was dried in a vacuum dryer at 90°C for 12 h.

2.3. Synthesis of WS_2/WO_3 NB Composite. The WS_2/WO_3 NB composite was also synthesized via the process used for WO_3 NR, with slight modifications. Initially, TAA (3.75 g) was dissolved and stirred for 30 min in DMF (25 mL) in a 100 mL Teflon beaker. Subsequently, AMT (4 g) was added to the prepared solution, followed by stirring continuously for 30 min. Then, the Teflon beaker was placed in a batch reactor system and heated at 180°C for 24 h. After cooling to room temperature, the precipitate was formed at the bottom of the Teflon beaker, and it was collected and centrifuged thrice with DI water. The obtained powder, WS_2/WO_3 NB, was dried in a vacuum dryer at 90°C for 12 h.

2.4. Synthesis of WS_2/WO_3 NR Heterostructure. The WS_2/WO_3 NR heterostructure was also synthesized via the technique used for WO_3 NR and WS_2/WO_3 NB, with slight modifications. Firstly, TAA (3.75 g) was dissolved and stirred for 30 min in DI water (25 mL) in a 100 mL Teflon beaker. Subsequently, AMT (4 g) was added to the prepared solution, followed by stirring continuously for 30 min. After that, 37% HCl (3 mL) was added to the Teflon beaker, followed by stirring continuously for 30 min. Then, the Teflon beaker was placed in a batch reactor system and heated at 180°C for 24 h. After cooling to room temperature, the precipitate was formed at the bottom of the Teflon beaker, and it was collected and centrifuged thrice with DI water. The obtained powder, WS_2/WO_3 NR, was dried in a vacuum dryer at 90°C for 12 h.

2.5. Electrochemical Measurements. The HER performance of different materials was evaluated by a three-electrode system (Ivium potentiostat V55630) using 0.5 M H_2SO_4 electrolyte solution. Graphite rod, saturated calomel, and catalyst-coated glassy carbon electrodes with diameters of 3 mm were used as the counter, reference, and working electrodes, respectively. The catalyst inks were prepared by mixing 1 mg of each powder with 1 mL of DMF water and 50 μL of Nafion (5%) which works as the stabilizer. The prepared inks were then drop coated on glassy carbon, followed by drying at 90°C for 30 min. Linear sweep voltammetry (LSV) was conducted to measure the HER performance (scan rate of 10 $mV\,s^{-1}$). To calculate the double layer capacitance (C_{dl}), the cyclic voltammetry measurements were investigated from 0 to 0.2 V at various scan rates of 10, 20, 30, 40, and 50 $mV\,s^{-1}$. Electrochemical impedance spectroscopy (EIS) was studied at a potential of 280 mV and frequencies ranging from 100 kHz to 0.1 Hz.

2.6. Material Characterization. The crystallinity of the synthesized materials was confirmed using X-ray diffraction (XRD, D8-Advance/Bruker-AXS). Additionally, Raman spectroscopy (LabRAM HR, Horiba Jobin Yvon) was also studied to confirm the structures of prepared materials. After that, the morphologies, sizes, and shapes of the synthesized materials were analyzed using field-emission scanning

electron microscopy (FE-SEM, SIGMA/Carl Zeiss). The chemical compositions as well as the oxidation states of the constituent elements of WO_3 NR, WS_2/WO_3 NB, and WS_2/WO_3 NR were then investigated by using X-ray photoelectron spectroscopy (XPS, Thermo Fisher Scientific, K-Alpha, USA).

2.7. Synthesis Process and Proposed Mechanisms. The proposed reaction mechanism of the synthesis process is shown in Figure 1.

(1) *Synthesis of WO_3 NR.* Source materials (AMT, TAA, and H_2O).

$$(NH_4)_6H_2W_{12}O_{40}.xH_2O \longrightarrow 6NH_3 + 8H^+ + [W_{12}O_{40}]^{8-} + xH_2O \quad (1)$$

$$CH_3CSNH_2 + 2H_2O \longrightarrow H_2S + NH_3 + H^+ + CH_3COO^- \quad (2)$$

$$[W_{12}O_{40}]^{8-} + 8H^+ \longrightarrow 12WO_3 + 4H_2O \quad (3)$$

(2) *Synthesis of WS_2/WO_3 NB Composite.* Source materials (AMT, TAA, and DMF).

$$(NH_4)_6H_2W_{12}O_{40}.xH_2O \longrightarrow 6NH_3 + 8H^+ + [W_{12}O_{40}]^{8-} + xH_2O \quad (4)$$

$$CH_3CSNH_2 + 2H_2O \longrightarrow H_2S + NH_3 + H^+ + CH_3COO^- \quad (5)$$

$$C_3H_7NO + 10H_2O \longrightarrow H^+ + COOH^- + (NH_4)_6NH \quad (6)$$

$$[W_{12}O_{40}]^{8-} + 8H^+ \longrightarrow 12WO_3 + 4H_2O \quad (7)$$

$$3WO_3 + 7H_2S \longrightarrow 3WS_2 + SO_2 + 7H_2O \quad (8)$$

(3) *Synthesis of WS_2/WO_3 NR Heterostructure.* Source materials (AMT, TAA, HCl, and H_2O).

$$(NH_4)_6H_2W_{12}O_{40}.xH_2O \longrightarrow 6NH_3 + 8H^+ + [W_{12}O_{40}]^{8-} + xH_2O \quad (9)$$

$$CH_3CSNH_2 + 2H_2O \longrightarrow H_2S + NH_3 + H^+ + CH_3COO^- \quad (10)$$

$$HCl \longrightarrow H^+ + Cl^- \quad (11)$$

$$[W_{12}O_{40}]^{8-} + 8H^+ \longrightarrow 12WO_3 + 4H_2O \quad (12)$$

$$3WO_3 + 7H_2S \longrightarrow 3WS_2 + SO_2 + 7H_2O \quad (13)$$

When hydrothermal or solvothermal processes are conducted to prepare materials in closed system, the reactions inside the batch reactor could take place and be highly complicated. Based on the source materials and their properties, the above-suggested mechanisms (1-13) could take place in batch reactor, depending on the source materials. Those processes take place in a closed system at a high temperature (180°C) for a long time (24 h). Using AMT, TAA, and different agents (H_2O, DMF, and H_2O+HCl), various gases could be released (H_2S, NH_3, SO_2, or even water vapour) in a small volume of reactor, which could significantly change the pH of the solution, the pressure inside of the batch reactor, and/or produce new ions. Those factors are the main reason which leads to the form of various structures and morphologies of synthesized materials [23, 61].

3. Results and Discussion

The crystallinity and structure of the synthesized materials were well investigated by using XRD measurement. In Figure 2, it is clear that all the peaks in the XRD pattern of WO_3 NR can be indexed to the monoclinic WO_3 (JCPDS Card No. 83-0950) and the hexagonal WO_3 (JCPDS Card No. 85-2460), as confirmed in a previous study [62, 63]. No other peaks could be observed in the XRD pattern of WO_3 NR which indicated that the high purity of WO_3 NR material was successfully synthesized. To confirm the appearance of WS_2 in WS_2/WO_3 NB and WS_2/WO_3 NR, the pure WS_2 was also synthesized by Teflon line autoclave as previous process [64]. The XRD pattern of pure WS_2 is provided in Figure S1. In the XRD pattern of WS_2/WO_3 NB, there are three peaks located at 29° (004), 32° (101), and 35° (102) which could be ascribed to the hexagonal phase of WS_2 (JCPDS Card No. 08-0237) [24]. The XRD intensity of WO_3 peaks in WS_2/WO_3 NB is lower than those of WO_3 NR, and those peaks could be ascribed to the orthorhombic phase of tungsten oxide hydrate $WO_3.H_2O$ which was confirmed in the previous study [48]. The XRD result indicates the mixed phase of WS_2 and WO_3, suggesting the coexistence of WS_2 and WO_3 in WS_2/WO_3 NB. In the XRD pattern of WS_2/WO_3 NR, there are also various peaks of WO_3 which are in line with the peaks of WO_3 NR as mentioned above. Besides that, there are two peaks of WS_2 located at 29° (004) and 35° (102). The XRD data indicated the successful synthesis of different catalysts including WO_3 NR, WS_2/WO_3 NB, and WS_2/WO_3 NR.

Figure 3 shows the Raman spectra of the synthesized WO_3 NR, WS_2/WO_3 NB, and WS_2/WO_3 NR. In the Raman spectrum of WO_3 NR, the strongest peak centered at 786 cm^{-1} corresponds to the stretching vibration of O–W–O bonds. The weak peak at 292 cm^{-1} is attributed to the bending vibration of W–O–W bonds [65]. The vibrational modes centered at 103 cm^{-1} correspond to the lattice modes of hexagonal WO_3 [66]. Furthermore, a shoulder peak appearing at 935 cm^{-1} is attributed to the –W=O bonds of the hexagonal WO_3 crystal [67, 68]. The Raman spectra of WS_2/WO_3 NB and WS_2/WO_3 NR reveal that both materials exhibit characteristic peaks at 264, 350, 418, 705, and 805 cm^{-1}. The peaks located at 264 cm^{-1} are assigned to the

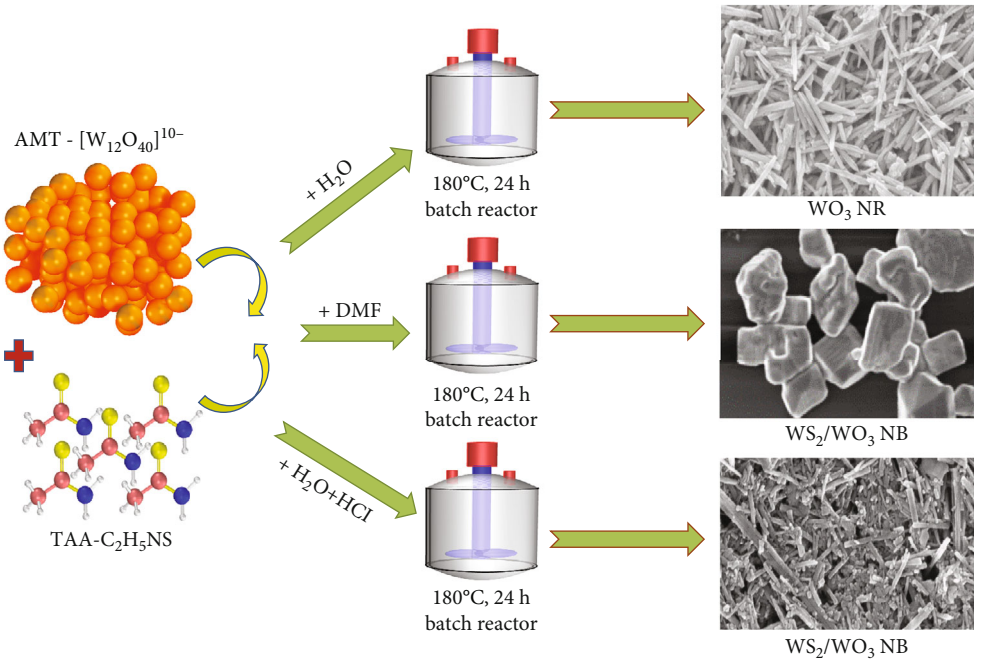

Figure 1: Syntheses of different structures of WO_3 and its derivatives.

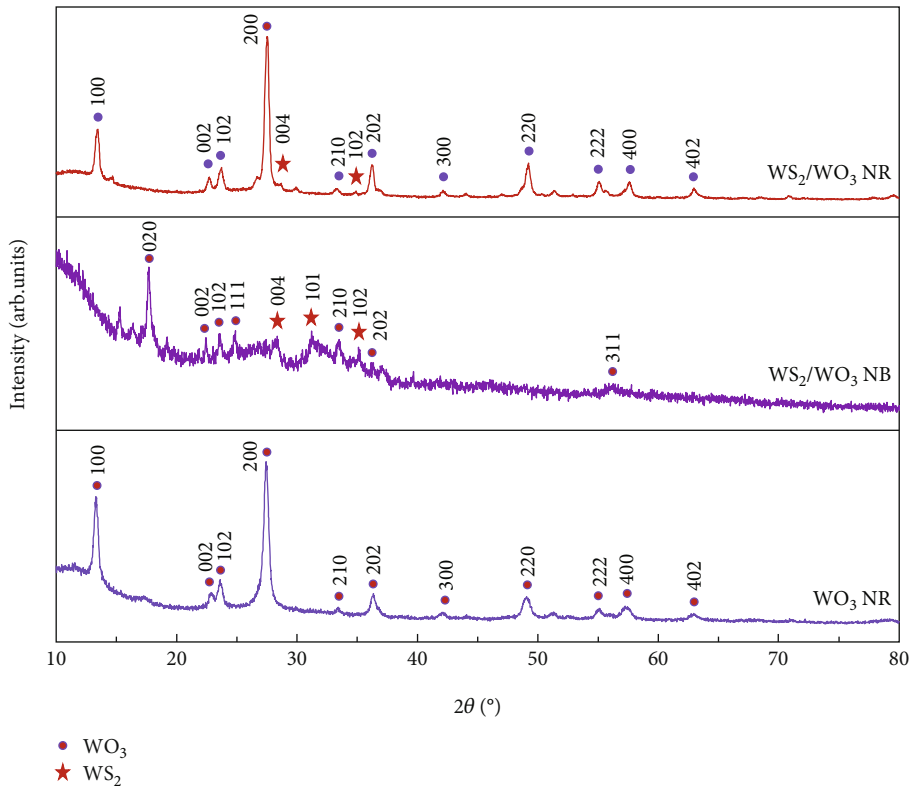

Figure 2: X-ray diffraction patterns of WO_3 NR, WS_2/WO_3 NB, and WS_2/WO_3 NR.

bending vibration of bridging oxygen of W–O–W bonds. The peaks located at approximately 705 and 805 cm^{-1} correspond to the stretching vibrations of the O–W–O bonds. The Raman peaks of WS_2 appear in the spectra of WS_2/WO_3 NB and WS_2/WO_3 NR. The peak position of the in-plane mode E^1_{2g} is located at approximately 350 cm^{-1}. For the interlayer

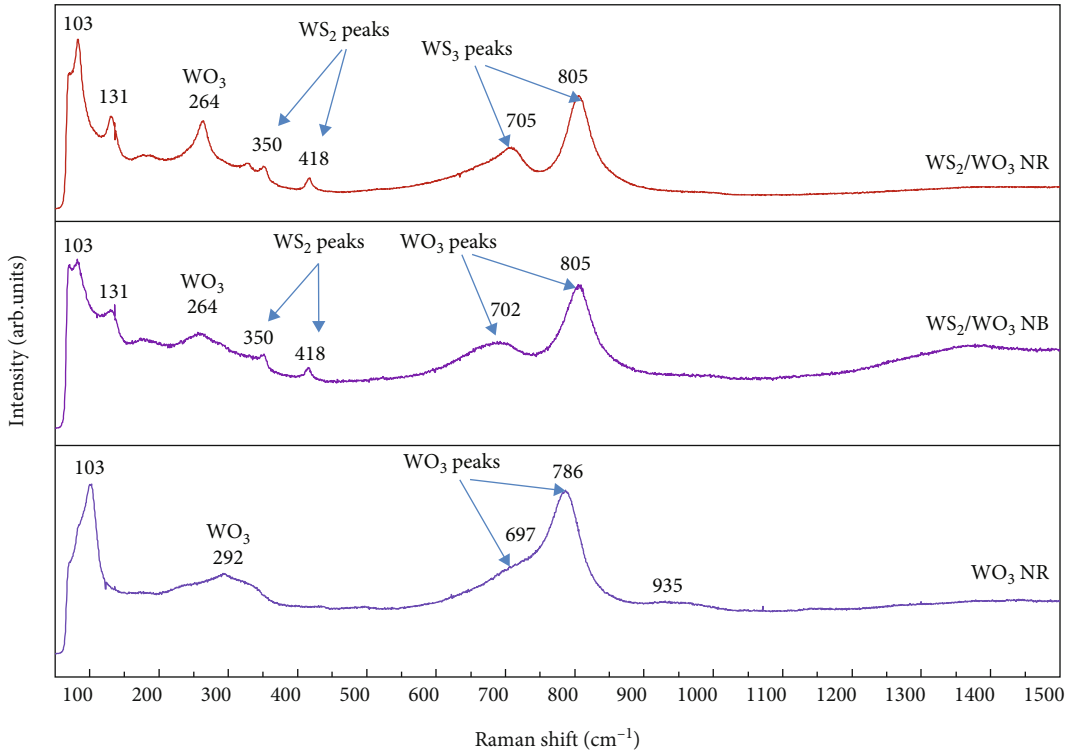

Figure 3: Raman spectra of WO_3 NR, WS_2/WO_3 NB, and WS_2/WO_3 NR.

vibration mode A_{1g}, the peaks are located at approximately 418 cm^{-1}, as reported in previous studies [69, 70]. The Raman spectra indicate that all the materials, namely, WO_3 NR, WS_2/WO_3 NB, and WS_2/WO_3 NR, were effectively synthesized.

XPS was used to study the chemical compositions of the material surfaces. Figure 4(a) shows the wide XPS spectra of WO_3 NR, WS_2/WO_3 NB, and WS_2/WO_3 NR. Peaks of W, S, O, and N are observed in all the synthesized materials, except for the absence of the S peak in the WO_3 NR spectrum. This result confirms that WO_3 NR, WS_2/WO_3 NB, and WS_2/WO_3 NR were successfully synthesized. The coincident appearance of nitrogen elements could be caused by using of AMT as a source of W which contains nitrogen elements. The presence of in-situ doped N_2 elements in catalysts could increase the contact of catalysts with electrolyte and improve the intrinsic conductivity of materials [71]. Figures 4(b), 4(d), and 4(f) depict the high-resolution fitted peaks of W 4f in WO_3 NR, WS_2/WO_3 NB, and WS_2/WO_3 NR, respectively. In Figure 4(b), the XPS spectrum of W 4f in WO_3 NR is deconvoluted into two main states, namely, W $4f_{7/2}$ and W $4f_{5/2}$, located at approximately 35.2 and 37.4 eV, respectively. The XPS data indicates that pure WO_3 NR was synthesized. In contrast, the XPS spectra of W 4f in WS_2/WO_3 NB and WS_2/WO_3 NR can be fitted into four different peaks, as shown in Figures 4(d) and 4(f), respectively. The peaks centered at approximately 31.8 and 33.9 eV are assigned to W (IV) of W–S bonding (WS_2), whereas those located at approximately 35.7 and 38 eV can be indexed to W (VI) of W–O bonding (WO_3). In addition, S peaks are observed only for the synthesized WS_2/WO_3 NB and WS_2/WO_3 NR. The high-resolution XPS peaks of S in the synthesized WS_2/WO_3 NB and WS_2/WO_3 NR are presented in Figures 4(c) and 4(e), respectively. In Figures 4(c) and 4(e), the main doublet of the binding energies of 161.6 and 162.8 eV in the high-resolution XPS peaks of S 2p is ascribed to the S $2p_{3/2}$ and S $2p_{1/2}$ states of the W–S bond in WS_2, respectively. Moreover, the peak located at approximately 168.7 eV corresponds to the S–O bond (SO_2), which is attributed to the inevitable oxidation of the composite in air [72]. The presence of WO_3 and WS_2 in XPS data confirms the successful synthesis of WS_2/WO_3 NB and WS_2/WO_3 NR.

Figure S2 shows the high-resolution XPS peaks of O 1 s in the synthesized materials including WO_3 NR, WS_2/WO_3 NB, and WS_2/WO_3 NR. The deconvoluted peaks of O 1 s in the synthesized materials are considerably similar, with slightly shifted peaks after fitting, which could be assigned to the different synthesized structures. All the O 1 s peaks can be fitted to two main peaks, wherein the higher peaks are assigned to the W–O–W bonding and the lower peaks correspond to the –OH groups owing to contamination or crystal water [73]. All the XPS data confirm that different materials such as WO_3 NR, WS_2/WO_3 NB, and WS_2/WO_3 NR were successfully synthesized.

The morphologies, sizes, and shapes of the prepared materials were investigated using FE-SEM at various scales. Figure 5 presents the FE-SEM images of WO_3 NR, WS_2/WO_3 NB, and WS_2/WO_3 NR. The sizes, shapes, and morphologies of the synthesized materials are highly uniform. In Figures 5(a) and 5(b), the length of WO_3 NR is

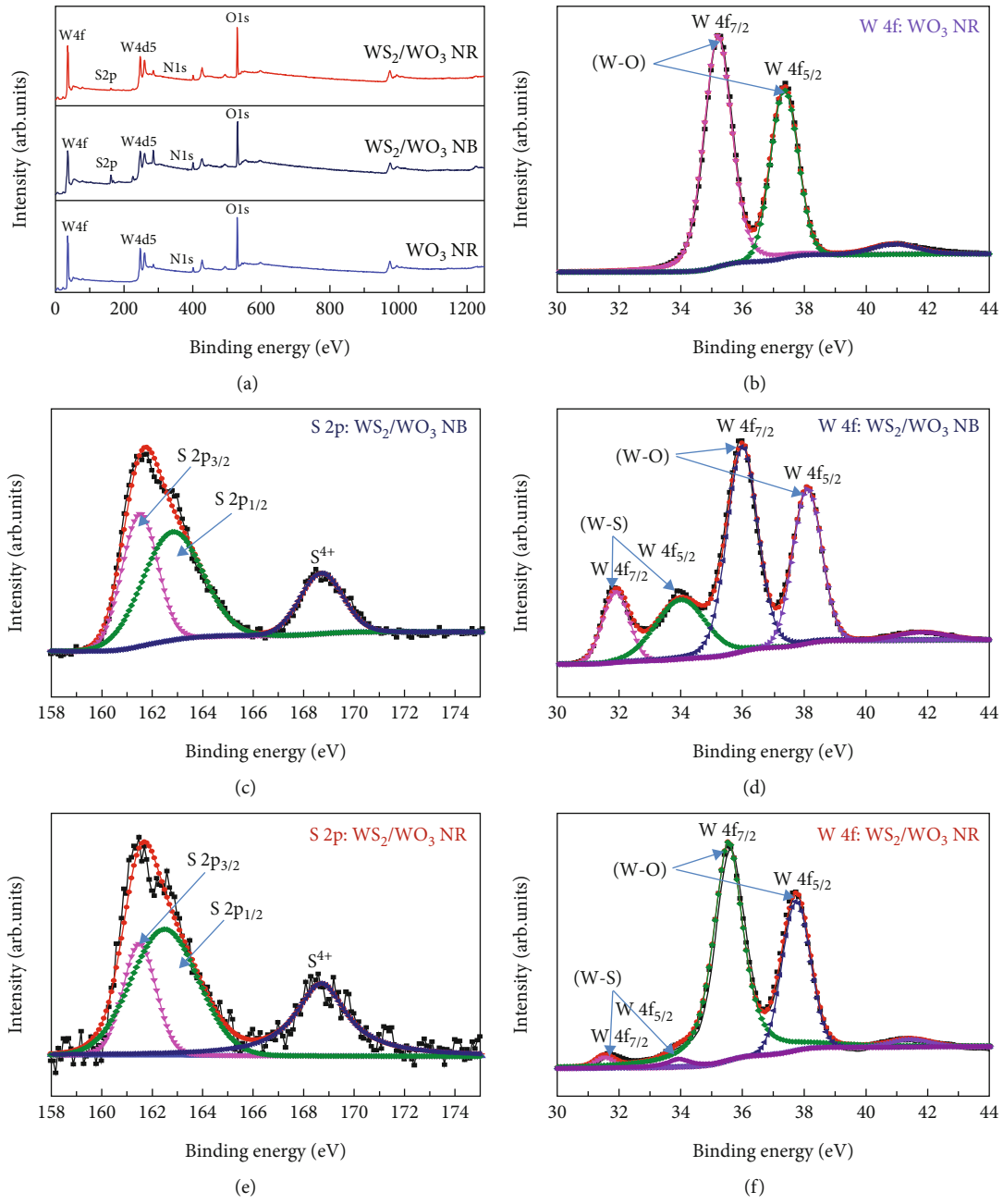

FIGURE 4: XPS survey spectra of the synthesized materials (a). High-resolution XPS spectra of W 4f in WO_3 NR (b), S 2p - W 4f in WS_2/WO_3 NB (c, d), and S 2p - W 4f in WS_2/WO_3 NR (e, f).

approximately 200–300 nm with a diameter of approximately 30–50 nm. In contrast, in Figures 5(c) and 5(d), the shape of WS_2/WO_3 NB appears in cubic shape, with dimensions of approximately 400 × 500 × 900 nm. As can be seen from Figures 5(e) and 5(f), it seems that the WS_2 layer covers the surface of the WO_3 NR material. The synthesized WS_2/WO_3 NR is highly uniform, with a length range of approximately 100–200 nm and a diameter range of approximately 15–30 nm. The FE-SEM data indicate that different morphologies of catalysts based on WO_3 have been well prepared.

During the HER, H_2 is released when protons (H^+) in the electrolyte receive electrons from an applied voltage on the electrode surface. The HER in acidic media involves the following steps:

$$H^+ + e^- \longrightarrow H_{ad} \quad \text{Volmer step} \tag{14}$$

$$H^+ + e^- + H_{ad} \longrightarrow H_2 \quad \text{Heyrovsky step} \tag{15}$$

$$H_{ad} + H_{ad} \longrightarrow H_2 \quad \text{Tafel step} \tag{16}$$

The efficiency of hydrogen evolution depends strongly on the electrode properties because hydrogen gas could be released on the cathode surface. Therefore, the more

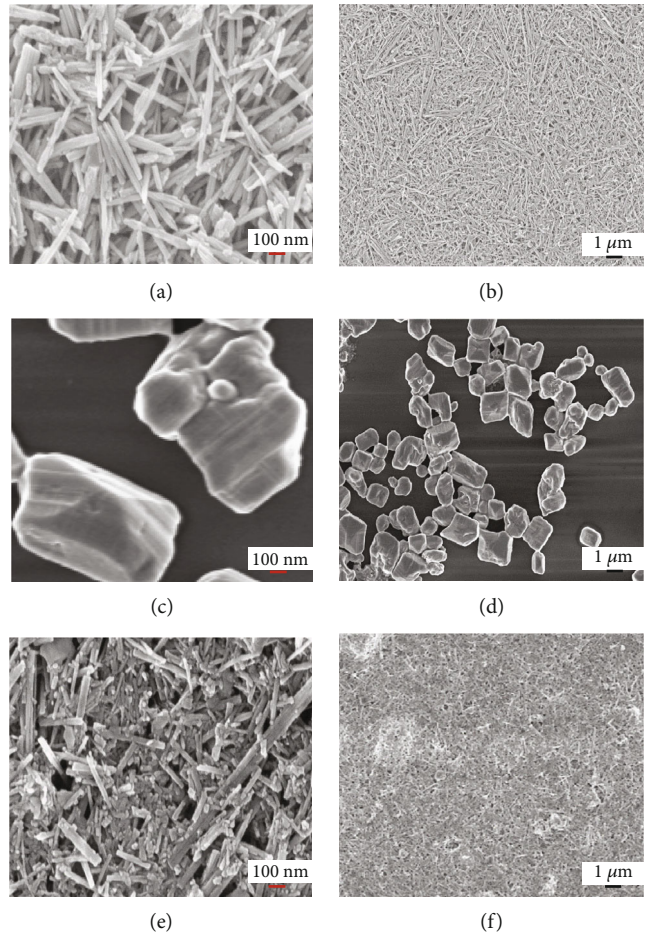

Figure 5: Field-emission scanning electron microscopy images of (a, b) WO_3 NR, (c, d) WS_2/WO_3 NB, and (e, f) WS_2/WO_3 NR.

conductive and larger the active surface of the catalysts, the higher the catalytic performance. Figure 6 shows the electrochemical measurements of all samples with reference to the HER performance. The LSV data clearly indicate the poor catalytic behavior of WS_2/WO_3 NB. This could be explained by the big size of the WS_2/WO_3 NB particles, as revealed by the FE-SEM results. The large size of the WS_2/WO_3 NB is the primary reason for its low conductivity and small active surface. In contrast, the WO_3 NR and WS_2/WO_3 NR samples exhibit good HER activities and higher current densities at lower overpotentials. The WO_3 NR and WS_2/WO_3 NB samples achieve a current density of 10 mA cm^{-2} at overpotentials of 284 and 394 mV, respectively. The WS_2/WO_3 NR sample attains the current density of 10 mA cm^{-2} at an overpotential of 224 mV, implying that the HER activity of WS_2/WO_3 NR is enhanced compared with that of WO_3 NR and WS_2/WO_3 NB. These results suggest that the heterostructure of WS_2 and WO_3 could play a crucial role in improving the HER activity in acidic media. The binary structure of WS_2 and WO_3 in the sample may create a synergistic effect that consequently increases the number of active sites and enhances the conductivity, thereby improving the HER performance [64, 74–77].

The Tafel slope is another important parameter for evaluating the catalytic activity of catalysts and is strongly related to the catalytic activity of the materials. The reaction mechanism and exchange current density were interpreted based on the calculated Tafel slopes. Figure 6(b) depicts the Tafel slopes of the synthesized materials. The Tafel slope of WS_2/WO_3 NR (82.7 mV dec^{-1}) is considerably smaller than that of WO_3 NR (112.5 mV dec^{-1}) and WS_2/WO_3 NB (195.5 mV dec^{-1}), which suggests that the HER kinetics of WS_2/WO_3 NR are faster than those of WO_3 NR and WS_2/WO_3 NB. In Figure 6(c), the EIS results derived from the recorded Nyquist plots reveal that WS_2/WO_3 NR presents a smaller semicircle diameter than that of WS_2/WO_3 NB and WO_3 NR, indicating the higher conductivity and charge-transfer rate and consequently the faster HER kinetics of WS_2/WO_3 NR. The equivalent circuit in the inset is composed of constant-phase elements and charge-transfer resistances. The fitted values are listed in Table 1. Notably, the charge-transfer resistance of WS_2/WO_3 NR (397.7 Ω) is considerably lower than that of WS_2/WO_3 NB (3597 Ω) and WO_3 NR (1816 Ω). Therefore, the electron conduction on the surface of WS_2/WO_3 NR is superior to that on WS_2/WO_3 NB and WO_3 NR. C_{dl} of WS_2/WO_3 NR was also calculated by using cyclic voltammetry (CV) tests at different scan rates. The CV test results of WS_2/WO_3 NR at various scan rates are shown in the inset of Figure 6(d). C_{dl} is calculated to be approximately 1.327 mF cm^{-2}, which is comparable

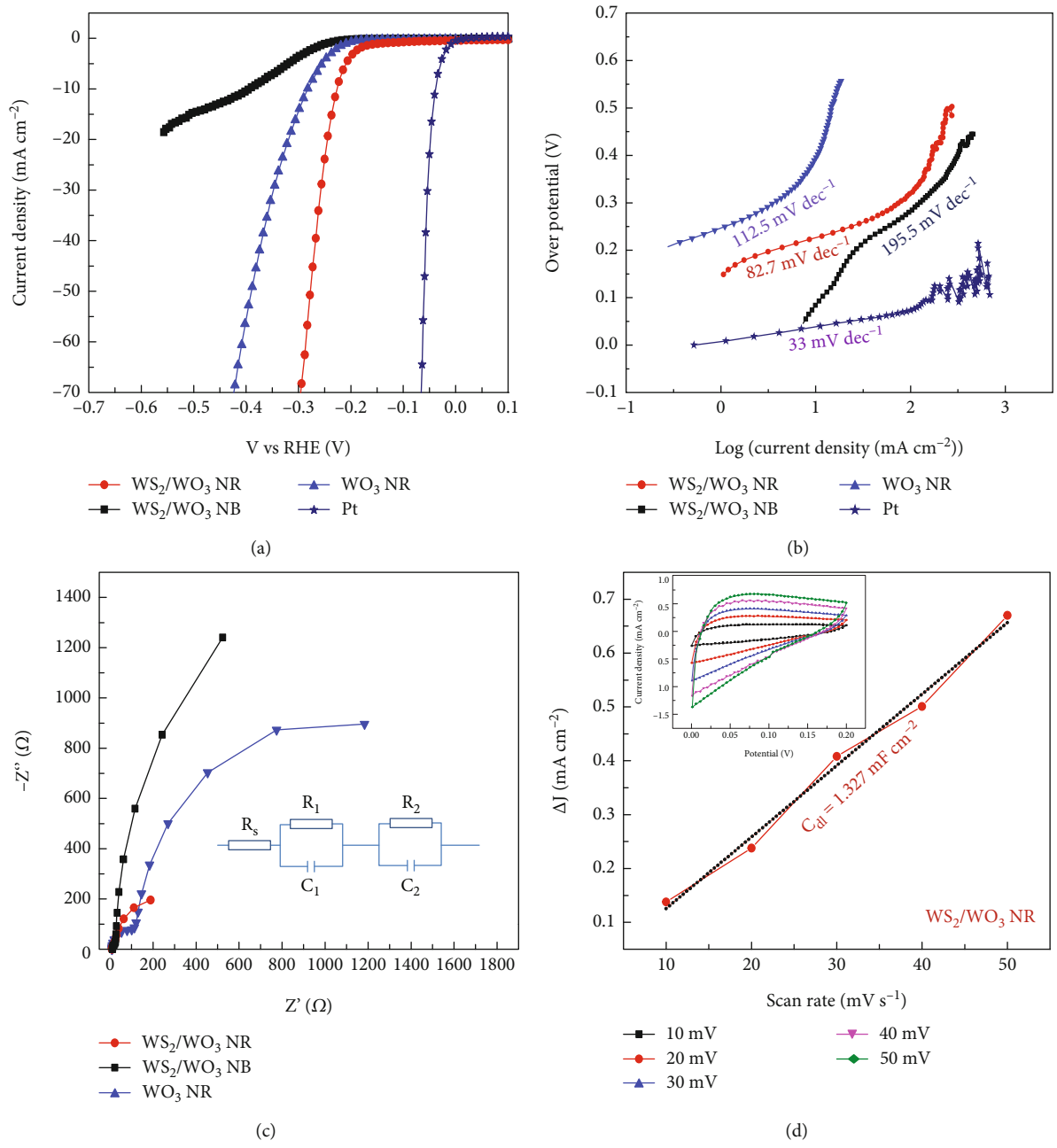

Figure 6: Hydrogen evolution reaction performance of WO_3 NR, WS_2/WO_3 NB, and WS_2/WO_3 NR compared with that of Pt. (a) Linear sweep voltammograms and (b) Tafel plots of the synthesized WO_3 NR, WS_2/WO_3 NB, and WS_2/WO_3 NR. (c) Electrochemical impedance spectroscopy plots of the synthesized WO_3 NR, WS_2/WO_3 NB, and WS_2/WO_3 NR. (d) C_{dl} of WS_2/WO_3 NR.

Table 1: Charge-transfer resistances of prepared materials.

Materials	R_s (Ω)	R_1 (Ω)	R_2 (Ω)
WO_3 NR	9.33	1816	11.2
WS_2/WO_3 NB	10.83	3597	16.22
WS_2/WO_3 NR	8.91	397.7	14.96

to that of WS_2 hollow spheres in a previous study [50]. The stability of WS_2/WO_3 NR was also investigated by i-t measurement for 12 h which is provided in Figure S3.

4. Conclusions

In summary, WO_3 NR, WS_2/WO_3 NB, and WS_2/WO_3 NR heterostructures were successfully synthesized using batch reactor routes. The structure, morphology, composition, and characteristics of the synthesized materials were completely confirmed. Subsequently, the HER performances of the prepared materials were thoroughly investigated. The catalytic activities of WS_2/WO_3 NR have been considerably improved compared with that of WO_3 NR and WS_2/WO_3 NB. The improved performance of WS_2/WO_3 NR heterostructures

could be attributed to the coexistence of WS_2 and WO_3 materials, which could create a synergistic effect between the two materials and further improve the conductivity and intrinsic HER activity. The Tafel slope of the WS_2/WO_3 NR (82.7 mV dec^{-1}) is considerably lower than that of pure WO_3 NR (112.5 mV dec^{-1}) or WS_2/WO_3 NB (195.5 mV dec^{-1}). Besides that, the long-time stability of prepared WS_2/WO_3 NR heterostructures was also confirmed. This study provides a prominent strategy for designing heterostructures of transition-metal sulfides/oxides based on WO_3 and WS_2 to prepare an efficient catalyst for electrochemical processes or energy-storage applications.

Data Availability

The data used to support the findings of this study are included within the manuscript and the supplementary information files.

Conflicts of Interest

The authors declare that they have no conflicts of interest.

Authors' Contributions

Tuan Van Nguyen and Kim Anh Huynh contributed equally to this work and co-first authors.

Acknowledgments

This research was supported by the NRF funded by the Korean government (2022M3H4A1A01012712 and 2022M3H4A1A04096380).

Supplementary Materials

Figure S1: XRD pattern of WS_2 material. Figure S2: (a) High-resolution XPS profiles of O 1 s in WO_3 NR, (b) WS_2/WO_3 NB, and (c) WS_2/WO_3 NR. Figure S3: stability test of WS_2/WO_3 nanorod catalyst by i-t measurement for 12 hours. Table S1: different catalysts based on WO_3 and/or WS_2 for HER. *(Supplementary Materials)*

References

[1] J. H. Cho, C. Lee, S. H. Hong et al., "Transition metal ion doping on ZIF-8 Enhances the electrochemical CO_2 Reduction reaction," *Advanced Materials*, vol. 35, no. 43, article 2208224, 2023.

[2] M. K. Lee, M. Shokouhimehr, S. Y. Kim, and H. W. Jang, "Two-dimensional metal–organic frameworks and covalent–organic frameworks for electrocatalysis: distinct merits by the reduced dimension," *Advanced Energy Materials*, vol. 12, no. 4, article 2003990, 2022.

[3] S. Kim, K. H. Kim, C. Oh, K. Zhang, and J. H. Park, "Artificial photosynthesis for high-value-added chemicals: old material, new opportunity," *Carbon Energy*, vol. 4, no. 1, pp. 21–44, 2022.

[4] M. Yue, H. Lambert, E. Pahon, R. Roche, S. Jemei, and D. Hissel, "Hydrogen energy systems: a critical review of technologies, applications, trends and challenges," *Renewable and Sustainable Energy Reviews*, vol. 146, article 111180, 2021.

[5] S. H. So, S. J. Sung, S. J. Yang, and C. R. Park, "Where to go for the development of high-performance H_2 storage materials at ambient conditions?," *Electronic Materials Letters*, vol. 19, no. 1, pp. 1–18, 2023.

[6] S. Hölzel, M. V. Zyuzin, J. Wallys et al., "Dynamic extracellular imaging of biochemical cell activity using InGaN/GaN nanowire arrays as nanophotonic probes," *Advanced Functional Materials*, vol. 28, no. 39, article 1802503, 2018.

[7] W. Wang, Y. Zheng, X. Li et al., "2D AlN layers sandwiched between graphene and Si substrates," *Advanced Materials*, vol. 31, no. 2, article e1803448, 2019.

[8] G. Loisch, Y. Chen, C. Koschitzki et al., "Direct measurement of photocathode time response in a high-brightness photoinjector," *Applied Physics Letters*, vol. 120, no. 10, 2022.

[9] X. Wang, G. Hai, B. Li, Q. Luan, W. Dong, and G. Wang, "Construction of dual-Z-scheme WS_2-$WO_3{\cdot}H_2O$/g-C_3N_4 catalyst for photocatalytic H_2 evolution under visible light," *Chemical Engineering Journal*, vol. 426, article 130822, 2021.

[10] X. Li, C. Garlisi, Q. Guan et al., "A review of material aspects in developing direct Z-scheme photocatalysts," *Materials Today*, vol. 47, pp. 75–107, 2021.

[11] S. Anwer, G. Bharath, S. Iqbal et al., "Synthesis of edge-site selectively deposited au nanocrystals on TiO_2 nanosheets: an efficient heterogeneous catalyst with enhanced visible-light photoactivity," *Electrochimica Acta*, vol. 283, pp. 1095–1104, 2018.

[12] A. Shoaib, M. Ji, H. Qian, J. Liu, M. Xu, and J. Zhang, "Noble metal nanoclusters and their in situ calcination to nanocrystals: precise control of their size and interface with TiO_2 nanosheets and their versatile catalysis applications," *Nano Research*, vol. 9, no. 6, pp. 1763–1774, 2016.

[13] N. Ullah and D. Guziejewski, "Formation of tungsten-doped molybdenum selenide electrocatalyst for methanol oxidation reaction," *Ionics*, vol. 29, no. 6, pp. 2523–2527, 2023.

[14] M. G. Lee, J. W. Yang, H. Park et al., "Crystal facet engineering of TiO_2 nanostructures for enhancing photoelectrochemical water splitting with $BiVO_4$ nanodots," *Nano-Micro Letters*, vol. 14, no. 1, p. 48, 2022.

[15] B. Jin, Y. Cho, C. Park et al., "A two-photon tandem black phosphorus quantum dot-sensitized $BiVO_4$ photoanode for solar water splitting," *Energy & Environmental Science*, vol. 15, no. 2, pp. 672–679, 2022.

[16] C. Tarhan and M. A. Çil, "A study on hydrogen, the clean energy of the future: hydrogen storage methods," *Journal of Energy Storage*, vol. 40, article 102676, 2021.

[17] B. R. Lee and H. W. Jang, "β-In_2S_3 as water splitting photoanodes: promise and challenges," *Electronic Materials Letters*, vol. 17, no. 2, pp. 119–135, 2021.

[18] Z. Yang, F. Shaik, K. Liang, K. Guo, X. Ren, and B. Jiang, "Self-supported phosphorus-doped vertically aligned graphene arrays integrated with FeCoNiP nanoparticles as bifunctional electrocatalysts for water-splitting over a wide pH range," *Electronic Materials Letters*, vol. 17, no. 1, pp. 87–101, 2021.

[19] D. Van Dao, G. Di Liberto, H. Ko et al., "$LaFeO_3$ meets nitrogen-doped graphene functionalized with ultralow Pt loading in an impactful Z-scheme platform for photocatalytic hydrogen evolution," *Journal of Materials Chemistry A*, vol. 10, no. 7, pp. 3330–3340, 2022.

[20] C. Liu, C. Kong, F. J. Zhang et al., "Research progress of defective MoS_2 for photocatalytic hydrogen evolution," *Journal of the Korean Ceramic Society*, vol. 58, no. 2, pp. 135–147, 2021.

[21] Y. Xu, M. Kraft, and R. Xu, "Metal-free carbonaceous electrocatalysts and photocatalysts for water splitting," *Chemical Society Reviews*, vol. 45, no. 11, pp. 3039–3052, 2016.

[22] T. Van Nguyen, T. P. Nguyen, Q. V. Le, D. V. Dao, S. H. Ahn, and S. Y. Kim, "Synthesis of very small molybdenum disulfide nanoflowers for hydrogen evolution reaction," *Applied Surface Science*, vol. 607, article 154979, 2023.

[23] T. Van Nguyen, M. Tekalgne, T. P. Nguyen et al., "Control of the morphologies of molybdenum disulfide for hydrogen evolution reaction," *International Journal of Energy Research*, vol. 46, no. 8, pp. 11479–11491, 2022.

[24] T. Van Nguyen, H. H. Do, M. Tekalgne et al., "WS_2–WC–WO_3 nano-hollow spheres as an efficient and durable catalyst for hydrogen evolution reaction," *Nano Convergence*, vol. 8, no. 1, p. 28, 2021.

[25] T. Van Nguyen, T. P. Nguyen, Q. V. le, D. V. Dao, S. H. Ahn, and S. Y. Kim, "Facile route for synthesizing WS_2/W_2C nano hollow flowers and their application for hydrogen evolution reaction," *Journal of Alloys and Compounds*, vol. 955, article 170231, 2023.

[26] C. M. Kai, C. Kong, F. J. Zhang, D. C. Li, Y. R. Wang, and W. C. Oh, "In situ growth of CdS spherical nanoparticles/Ti_3C_2 MXene nanosheet heterojunction with enhanced photocatalytic hydrogen evolution," *Journal of the Korean Ceramic Society*, vol. 59, no. 3, pp. 302–311, 2022.

[27] A. Kumar, I. H. Kim, L. Mathur, H. S. Kim, and S. J. Song, "Design of tin polyphosphate for hydrogen evolution reaction and supercapacitor applications," *Journal of the Korean Ceramic Society*, vol. 58, no. 6, pp. 688–699, 2021.

[28] J. Lin, W. Wang, and G. Li, "Modulating surface/interface structure of emerging InGaN nanowires for efficient photoelectrochemical water splitting," *Advanced Functional Materials*, vol. 30, no. 52, article 2005677, 2020.

[29] C. Li and J. B. Baek, "Recent advances in noble metal (Pt, Ru, and Ir)-based electrocatalysts for efficient hydrogen evolution reaction," *ACS Omega*, vol. 5, no. 1, pp. 31–40, 2020.

[30] S. Kumar, P. K. Sahoo, and A. K. Satpati, "Insight into the catalytic performance of HER catalysis of noble metal/3D-G nanocomposites," *Electrochimica Acta*, vol. 333, article 135467, 2020.

[31] N. Han, K. R. Yang, Z. Lu et al., "Nitrogen-doped tungsten carbide nanoarray as an efficient bifunctional electrocatalyst for water splitting in acid," *Nature Communications*, vol. 9, no. 1, p. 924, 2018.

[32] F. Almomani, A. Al-Rababah, M. Tawalbeh, and A. Al-Othman, "A comprehensive review of hydrogen generation by water splitting using 2D nanomaterials: photo vs electro-catalysis," *Fuel*, vol. 332, article 125905, 2023.

[33] T. Van Nguyen, M. Tekalgne, T. P. Nguyen, Q. Van Le, S. H. Ahn, and S. Y. Kim, "Electrocatalysts based on $_{MoS2and}$ WS2for hydrogen evolution reaction: an overview," *Battery Energy*, vol. 2, no. 3, article 20220057, 2023.

[34] L. Xiong, Y. Qiu, X. Peng, Z. Liu, and P. K. Chu, "Electronic structural engineering of transition metal-based electrocatalysts for the hydrogen evolution reaction," *Nano Energy*, vol. 104, article 107882, 2022.

[35] F. J. Zhang, C. Kong, X. Li, X. Y. Sun, W. J. Xie, and W. C. Oh, "Synthesis and characterization of MoS_2/graphene-TiO_2 ternary photocatalysts for high-efficiency hydrogen production under visible light," *Journal of the Korean Ceramic Society*, vol. 56, no. 3, pp. 284–290, 2019.

[36] D. Shin, H. W. Shim, B. Swain, K. S. Park, and C. G. Lee, "Facile synthesis of single-phase alpha-tungsten nanopowders from ammonium paratungstate by RF induction thermal plasma and thermochemical reduction," *Korean Journal of Metals and Materials*, vol. 58, no. 11, pp. 798–807, 2020.

[37] J. Kim, M. Kim, C. Y. Seo et al., "Effects of Al, V, Cr, Mn, Ni, Nb, Mo, and W addition to BCC-Fe on its elastic properties and hardness for a biomass boiler: first principles approaches," *Korean Journal of Metals and Materials*, vol. 57, no. 6, pp. 374–380, 2019.

[38] D. K. Lee, S. J. Wee, K. J. Jang et al., "3D-printed cobalt-rich tungsten carbide hierarchical electrode for efficient electrochemical ammonia production," *Journal of the Korean Ceramic Society*, vol. 58, no. 6, pp. 679–687, 2021.

[39] T. Van Nguyen, H. H. Do, T. Q. Trung et al., "Stable and multicolored electrochromic device based on polyaniline-tungsten oxide hybrid thin film," *Journal of Alloys and Compounds*, vol. 882, article 160718, 2021.

[40] T. V. Nguyen, K. A. Huynh, Q. V. Le, H. Kim, S. H. Ahn, and S. Y. Kim, "Highly stable electrochromic cells based on amorphous tungsten oxides prepared using a solution-annealing process," *International Journal of Energy Research*, vol. 45, no. 5, pp. 8061–8072, 2021.

[41] T. Van Nguyen, H. H. Do, W. Guo et al., "Tungsten oxide-modified ITO electrode for electrochromic window based on reversible metal electrodeposition," *Electronic Materials Letters*, vol. 18, no. 1, pp. 36–46, 2022.

[42] A. Staerz, S. Somacescu, M. Epifani, T. Kida, U. Weimar, and N. Barsan, "WO_3-based gas sensors: identifying inherent qualities and understanding the sensing mechanism," *ACS Sensors*, vol. 5, no. 6, pp. 1624–1633, 2020.

[43] X. Li, X. Li, Z. Li, J. Wang, and J. Zhang, "WS_2 nanoflakes based selective ammonia sensors at room temperature," *Sensors and Actuators B: Chemical*, vol. 240, pp. 273–277, 2017.

[44] H. Zheng, Y. Tachibana, and K. Kalantar-Zadeh, "Dye-sensitized solar cells based on WO_3," *Langmuir*, vol. 26, no. 24, pp. 19148–19152, 2010.

[45] M. K. S. B. Rafiq, N. Amin, H. F. Alharbi et al., "WS_2: a new window layer material for solar cell application," *Scientific Reports*, vol. 10, no. 1, p. 771, 2020.

[46] Y. Zhong, Y. Shao, B. Huang, X. Hao, and Y. Wu, "Combining ZnS with WS_2 nanosheets to fabricate a broad-spectrum composite photocatalyst for hydrogen evolution," *New Journal of Chemistry*, vol. 41, no. 21, pp. 12451–12458, 2017.

[47] N. Li, H. Teng, L. Zhang, J. Zhou, and M. Liu, "Synthesis of Mo-doped WO_3 nanosheets with enhanced visible-light-driven photocatalytic properties," *RSC Advances*, vol. 5, no. 115, pp. 95394–95400, 2015.

[48] A. K. Nayak, M. Verma, Y. Sohn, P. A. Deshpande, and D. Pradhan, "Highly active tungsten oxide nanoplate electrocatalysts for the hydrogen evolution reaction in acidic and near neutral electrolytes," *ACS Omega*, vol. 2, no. 10, pp. 7039–7047, 2017.

[49] A. Phuruangrat, D. J. Ham, S. J. Hong, S. Thongtem, and J. S. Lee, "Synthesis of hexagonal WO_3 nanowires by microwave-assisted hydrothermal method and their electrocatalytic activities for hydrogen evolution reaction," *Journal of Materials Chemistry*, vol. 20, no. 9, pp. 1683–1690, 2010.

[50] T. P. Nguyen, D. L. T. Nguyen, V. H. Nguyen et al., "Facile synthesis of WS_2 hollow spheres and their hydrogen evolution reaction performance," *Applied Surface Science*, vol. 505, article 144574, 2020.

[51] M. A. Tekalgne, A. Hasani, D. Y. Heo et al., "SnO_2@WS_2/p-Si heterostructure photocathode for photoelectrochemical hydrogen production," *The Journal of Physical Chemistry C*, vol. 124, no. 1, pp. 647–652, 2020.

[52] Y. H. Li, P. F. Liu, L. F. Pan et al., "Local atomic structure modulations activate metal oxide as electrocatalyst for hydrogen evolution in acidic water," *Nature Communications*, vol. 6, no. 1, p. 8064, 2015.

[53] H. Tian, X. Cui, L. Zeng, L. Su, Y. Song, and J. Shi, "Oxygen vacancy-assisted hydrogen evolution reaction of the Pt/WO_3 electrocatalyst," *Journal of Materials Chemistry A*, vol. 7, no. 11, pp. 6285–6293, 2019.

[54] B. Cole, B. Marsen, E. Miller et al., "Evaluation of nitrogen doping of tungsten oxide for photoelectrochemical water splitting," *The Journal of Physical Chemistry C*, vol. 112, no. 13, pp. 5213–5220, 2008.

[55] Y. H. Xiao, C. Q. Xu, and W. D. Zhang, "Facile synthesis of Ni-doped WO_3 nanoplate arrays for effective photoelectrochemical water splitting," *Journal of Solid State Electrochemistry*, vol. 21, no. 11, pp. 3355–3364, 2017.

[56] D. Kong, H. Wang, Z. Lu, and Y. Cui, "$CoSe_2$ nanoparticles grown on carbon fiber paper: an efficient and stable electrocatalyst for hydrogen evolution reaction," *Journal of the American Chemical Society*, vol. 136, no. 13, pp. 4897–4900, 2014.

[57] X. Ge, L. Chen, L. Zhang, Y. Wen, A. Hirata, and M. Chen, "Nanoporous metal enhanced catalytic activities of amorphous molybdenum sulfide for high-efficiency hydrogen production," *Advanced Materials*, vol. 26, no. 19, pp. 3100–3104, 2014.

[58] G. Mineo, M. Scuderi, E. Bruno, and S. Mirabella, "Engineering hexagonal/monoclinic WO_3 phase junctions for improved electrochemical hydrogen evolution reaction," *ACS Applied Energy Materials*, vol. 5, no. 8, pp. 9702–9710, 2022.

[59] C. Xie, W. Chen, S. Du et al., "In-situ phase transition of WO_3 boosting electron and hydrogen transfer for enhancing hydrogen evolution on Pt," *Nano Energy*, vol. 71, article 104653, 2020.

[60] P. Zhou, Q. Xu, H. Li et al., "Fabrication of two-dimensional lateral heterostructures of WS_2/WO_3·H_2O through selective oxidation of monolayer WS_2," *Angewandte Chemie*, vol. 127, no. 50, pp. 15441–15445, 2015.

[61] N. Ullah, D. Guziejewski, K. Koszelska et al., "Formation mechanism of macroporous cu/CuSe and its application as electrocatalyst for methanol oxidation reaction," *Ionics*, vol. 29, no. 11, pp. 4835–4840, 2023.

[62] A. S. Hammad, H. M. El-Bery, A. H. El-Shazly, and M. F. Elkady, "Effect of WO_3 morphological structure on its photoelectrochemical properties," *International Journal of Electrochemical Science*, vol. 13, no. 1, pp. 362–372, 2018.

[63] H. T. Masood, S. Anwer, S. A. Rouf et al., "Back contact buffer layer of WO_3 nanosheets in thin-film CdTe solar cell," *Journal of Alloys and Compounds*, vol. 887, article 161367, 2021.

[64] A. Mahmood, S. Khan, F. Rahayu et al., "Factors effecting and structural engineering of molybdenum nitride-based electrocatalyst for overall water splitting: a critical review," *Energy Technology*, vol. 11, no. 7, article 2300182, 2023.

[65] R. Senthilkumar, G. Ravi, C. Sekar, M. Arivanandhan, M. Navaneethan, and Y. Hayakawa, "Determination of gas sensing properties of thermally evaporated WO_3 nanostructures," *Journal of Materials Science: Materials in Electronics*, vol. 26, no. 3, pp. 1389–1394, 2015.

[66] Y. Zheng, G. Chen, Y. Yu, Y. Hu, Y. Feng, and J. Sun, "Urea-assisted synthesis of ultra-thin hexagonal tungsten trioxide photocatalyst sheets," *Journal of Materials Science*, vol. 50, no. 24, pp. 8111–8119, 2015.

[67] W. Song, R. Zhang, X. Bai, Q. Jia, and H. Ji, "Exposed crystal facets of WO_3 nanosheets by phase control on NO_2-sensing performance," *Journal of Materials Science: Materials in Electronics*, vol. 31, no. 1, pp. 610–620, 2020.

[68] F. Zheng, M. Zhang, and M. F. Guo, "Controllable preparation of WO_3 nanorod arrays by hydrothermal method," *Thin Solid Films*, vol. 534, pp. 45–53, 2013.

[69] X. H. Wang, C. C. Zheng, and J. Q. Ning, "Influence of curvature strain and Van der Waals force on the inter-layer vibration mode of WS_2 nanotubes: a confocal micro-Raman spectroscopic study," *Scientific Reports*, vol. 6, no. 1, article 33091, 2016.

[70] C. Lee, B. G. Jeong, S. J. Yun, Y. H. Lee, S. M. Lee, and M. S. Jeong, "Unveiling defect-related Raman mode of monolayer WS_2 via tip-enhanced resonance Raman scattering," *ACS Nano*, vol. 12, no. 10, pp. 9982–9990, 2018.

[71] C. Sun, J. Zhang, J. Ma et al., "N-doped WS_2 nanosheets: a high-performance electrocatalyst for the hydrogen evolution reaction," *Journal of Materials Chemistry A*, vol. 4, no. 29, pp. 11234–11238, 2016.

[72] S. Lu, W. Luo, Z. Chao, Y. Liu, S. Han, and J. Fan, "A novel honeycomb-like WS_{2-x}/CoS@C composite as anode for lithium ion batteries," *Journal of Materials Science*, vol. 57, no. 8, pp. 5118–5129, 2022.

[73] R. Ji, D. Zheng, C. Zhou, J. Cheng, J. Yu, and L. Li, "Low-temperature preparation of tungsten oxide anode buffer layer via ultrasonic spray pyrolysis method for large-area organic solar cells," *Materials*, vol. 10, no. 7, p. 820, 2017.

[74] K. Xu, F. Wang, Z. Wang et al., "Component-controllable $WS_{2(1-x)}Se_{2x}$ nanotubes for efficient hydrogen evolution reaction," *ACS Nano*, vol. 8, no. 8, pp. 8468–8476, 2014.

[75] C. Tang, W. Wang, A. Sun et al., "Sulfur-decorated molybdenum carbide catalysts for enhanced hydrogen evolution," *ACS Catalysis*, vol. 5, no. 11, pp. 6956–6963, 2015.

[76] X. Shang, Y. Rao, S. S. Lu et al., "Novel WS_2/WO_3 heterostructured nanosheets as efficient electrocatalyst for hydrogen evolution reaction," *Materials Chemistry and Physics*, vol. 197, pp. 123–128, 2017.

[77] N. Ullah, M. Xie, S. Hussain et al., "Simultaneous synthesis of bimetallic@ 3D graphene electrocatalyst for HER and OER," *Frontiers of Materials Science*, vol. 15, no. 2, pp. 305–315, 2021.